REPORT DOCUMENTATION PAGE

AFRL-SR-BL-TR-98-

0091

1. AGENCY USE ONLY (*Leave Blank*)	2. REPORT DATE	3. REPORT TYPE AND DATES COVERED
	14 January 1998	Final 15 April 1994-14 November 1997

4. TITLE AND SUBTITLE
Time Accurate Computation Of Unsteady Hypersonic Inlet Flows with a Dynamic Flow Adaptive Mesh

5. FUNDING NUMBERS
F49620-94-1-0237

6. AUTHORS
D. Scott McRae
Michael Neaves

7. PERFORMING ORGANIZATION NAME(S) AND ADDRESS(ES)
North Carolina State University
Department of Mechanical and Aerospace Engineering
Box 7910
Raleigh, NC 27695-7910

8. PERFORMING ORGANIZATION REPORT NUMBER

9. SPONSORING / MONITORING AGENCY NAME(S) AND ADDRESS(ES)
Dr. Len Sakell
Air Force Office of Scientific Research
AFOSR/NM
Bolling AFB, DC 20332-6448

10. SPONSORING / MONITORING AGENCY REPORT NUMBER

11. SUPPLEMENTARY NOTES

12a. DISTRIBUTION / AVAILABILITY STATEMENT
Unlimited

12b. DISTRIBUTION CODE

13. ABSTRACT *(Maximum 200 words)*

Completed research is reported for an dynamic numerical investigation of unsteady flow in supersonic and hypersonic aircraft inlets. An explicit dynamic solution adaptive mesh computational code was further developed and used to obtain dynamic solutions for an axisymmetric mixed compression inlet and a generic dual-mode scramjet inlet-isolator-diffuser combination. To improve robustness, an existing implicit code was modified for time accuracy and the solution adaptive mesh algorithm was installed. The inlet unstart phenomenon was simulated through perturbation of freestream and downstream conditions (axisymmetric inlet) and through downsream throttling for the dual mode 3-D configuration. Axisymmetric unstart could be induced by a 10% freestream temperature increase or a 5% backpressure increase. Comparison of the results with experiment, where available, indicate that stability margins assessed through inviscid design or quasi-steady experiment may need revision when dynamics are considered. Conclusions are drawn concerning specifics of the flow phenomena and directions for future research are suggested. Lack of highly resolved dynamic experimental data is a pacing item and will prevent full verification of future work.

14. SUBJECT TERMS
Inlet unstart, computational fluid dynamics, hypersonic inlet

15. NUMBER OF PAGES
36

16. PRICE CODE

17. SECURITY CLASSIFICATION OF REPORT	18. SECURITY CLASSIFICATION OF THIS PAGE	19. SECURITY CLASSIFICATION OF ABSTRACT	20. LIMITATION OF ABSTRACT
unclassified	unclassified	unclassified	unlimited distr.

NSN 7540-01-280-5500

Standard Form 298 (Rev. 2-89)
Prescribed by ANSI Std. Z39-1
298-102

19980129 072

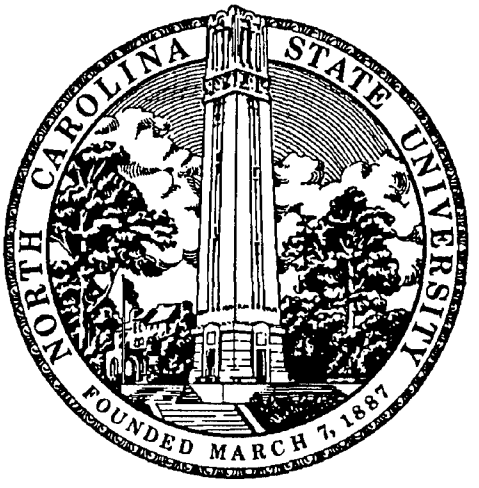

TIME ACCURATE COMPUTATION OF UNSTEADY HYPERSONIC INLET FLOWS WITH A DYNAMIC FLOW ADAPTIVE MESH

D. Scott McRae
Michael Neaves

Department of Mechanical and Aerospace Engineering
North Carolina State University
Raleigh, North Carolina 27695-7910

13 January 1998

Final Technical Report for Period 15 April 1994 to 14 Nov 1997
AFOSR Grant F49620-94-1-0237

Prepared for

Air Force Office of Scientific Research
AFOSR/NA
Bolling AFB, D. C. 20332-6448

Abstract

Completed research is reported for an dynamic numerical investigation of unsteady flow in supersonic and hypersonic aircraft inlets. An explicit dynamic solution adaptive mesh computational code was further developed and used to obtain dynamic solutions for an axisymmetric mixed compression inlet and a generic dual-mode scramjet inlet-isolator-diffuser combination. To improve robustness, an existing implicit code was modified for time accuracy and the solution adaptive mesh algorithm was installed. The inlet unstart phenomenon was simulated through perturbation of freestream and downstream conditions (axisymmetric inlet) and through downsream throttling for the dual mode 3-D configuration. Axisymmetric unstart could be induced by a 10% freestream temperature increase or a 5% backpressure increase. Comparison of the results with experiment, where available, indicate that stability margins assessed through inviscid design or quasi-steady experiment may need revision when dynamics are considered. Conclusions are drawn concerning specifics of the flow phenomena and directions for future research are suggested. Lack of highly resolved dynamic experimental data is a pacing item and will prevent full verification of future work.

Introduction

The majority of published studies, in which supersonic combustion ram jet (scramjet) propulsion systems were analyzed, have been for steady or quasi-steady simulation conditions (Weir, et al. (1989), Holland (1991), Benson (1986), Singh, et al. (1992), and Kerrebrock (1992)). In actual hypersonic aircraft applications, conditions will be far from steady. Therefore, techniques must be developed to simulate dynamically these systems so that their performance under actual operating conditions can be assessed prior to final design. Dynamic simulations will prevent expensive errors and will also increase design confidence prior to prototype construction.

Scramjet propulsion systems exhibit strong interaction between components. As noted in Kerrebrock (1992), a 1.5% drop in kinetic energy efficiency in the inlet can reduce I_{sp} by as much as 50% at higher velocities and at a given nozzle freezing pressure. Given that variation in freestream conditions must inevitably occur due to atmospheric and aircraft attitude change and that combustion chamber conditions must change with throttle setting, it is clear that the propulsion system as a whole must be considered both statically and dynamically.

The first step in assessing the dynamic interaction of the propulsion system components must be to develop means for analyzing the unsteady operation of the inlet section. The requirement that the inlet operate constantly at peak efficiency and that it maintain stable, mixed-compression flow during aircraft maneuver, atmospheric variations and combustion changes, leads to conflicting design parameters. Since the most efficient operating conditions are usually those closest to the unstable points, techniques used to design, evaluate and analyze the hypersonic inlet must be very accurate and must simulate the dynamic response of the inlet. A standard design technique that may (for instance) neglect viscous and unsteady effects is not likely to provide sufficient fidelity to reduce the design space with confidence. Also, the consequences of failing to assess properly an unstable mode in inlet operation can be very severe. A hypersonic inlet unstart can result in loss of 50% to 90% thrust in one or more modules (if adjacent) in a matter of milliseconds. The possibility of aircraft departure from stable flight upon inlet unstart becomes a strong possibility, given cross coupling effects. The issue is further exacerbated by the fact that

standard means of stabilizing SST type mixed compression inlets are practical only at the low end of the hypersonic range. All of these factors lead to an initial goal of developing an accurate inlet analysis techniques so the results of the design process can be evaluated under realistic conditions.

Completed work is reported herein for development of such an analysis tool. The remainder of this report details initial code development work in 2-D and development of the two 3-D codes used to compute dynamic flow through a generic hydrocarbon fuel inlet-isolator-diffuser configuration that Emami, et al. (1995) tested in the Mach 4 Blow Down Facility (M4BDF) at NASA Langley Research Center. Computational results are compared with experiment and conclusions are reported.

Numerical Procedure

The governing equations of fluid flow can be expressed in either integral or differential form. The integral statement for conservation of a dependent variable U over a domain $\mathcal{V}$ when generalized for changing $\mathcal{V}$ becomes

$$\frac{\partial}{\partial t}\int_{\mathcal{V}} U\, d\mathcal{V} - \oint_S U\, \dot{\vec{x}} \cdot d\vec{S} + \oint_S \vec{A} \cdot d\vec{S} = 0 \tag{1}$$

where $$U = [\rho, \rho\vec{V}, E_t]^T$$

and $$\vec{A} = E\hat{i} + F\hat{j} + G\hat{k}; \quad E = E(U), etc.; \quad \dot{\vec{x}} = \dot{x}\hat{i} + \dot{y}\hat{j} + \dot{z}\hat{k}.$$

The first and last integrals in Equation (1) are the standard forms that we normally encounter. The second integral is the correction to the conserved quantity for the gain/loss due to movement of the cell sides independently of the fluid velocity. The value of the second integral in Equation (1) for each cell is the sum of the conserved quantity U contained in the volume swept by the cell faces as the grid translates.

Two approaches for solving this equation were used in this research. In the first case, the discrete conservation equation is split into two steps. In the second, the equation is integrated in one step. Both methods will be described in turn and use variations of the adaptive mesh process,

DSAGA, from the original algorithm of Benson (1991), with modifications derived from SIERRA (Laflin (1997)).

Implementation of Time Accurate Explicit Algorithm

The split form of the algorithm can be expressed as follows, using a multistage Runge-Kutta time-stepping algorithm for solution Step (1) where *i* indicates the *i* th stage of the multi-stage Runge-Kutta algorithm

Step (1)

$$U^{(i)} = U^{(i-1)} - \alpha^{(i)} \frac{\Delta t}{\Psi^n} \left\{ \Delta_\xi \hat{E}^{(i-1)} + \Delta_\eta \hat{F}^{(i-1)} + \Delta_\zeta \hat{G}^{(i-1)} \right\} \tag{2}$$

The mesh is then adapted to the results of this step. The final step is (where (2) indicates the results of Step (1)):

Step (2)

$$(U\Psi)^{n+1} = \Psi^n U^{(2)} + \left\{ \Delta_\xi (U^{(2)} \Delta^n \Psi) + \Delta_\eta (U^{(2)} \Delta^n \Psi) + \Delta_\zeta (U^{(2)} \Delta^n \Psi) \right\} \tag{3}$$

In this equation, the term $\Delta^n \Psi$ represents the change in volume between the *n* and *n*+1 time level. As a cautionary note, care must be taken to insure that $\Delta^n \Psi$ includes all of the swept volume. If this final step is carried out with sufficient accuracy, the result will be the solution obtained at Step (1) expressed on a grid that will give very high spatial resolution for the next application of Step (1).

The steps of DSAGA as initially developed are as follows:

1) Use an available grid generator (preferably elliptical partial differential equation based) to obtain an initial structured, body-fitted grid.

2) Obtain the numerical approximations to the metric derivatives which define numerically a one-to-one transformation to a parametric space. These initial transformation metrics and their approximations remain temporally fixed.

3) A discrete source-term distribution is obtained based on selected parameters and criteria. This step is crucial to successful adaptation.

4) The discrete source term distribution is input to the Poisson solver (in this case Eiseman's "mass weighted algorithm") to find new solution dependent node locations.

5) The new grid node locations are then used to find a "grid velocity" (finite difference) or input to a finite volume redistribution algorithm (split or unsplit conservation law). In either case, the final step results in a solution at the n+1 time step on a grid that has been adapted to the chosen criteria at the n or n+1 time level.

Step 3) involves first selecting the solution parameters and/or features that require increased resolution. Two obvious candidates are viscous layers and shock waves (note that any solution feature can be chosen). Once these features are chosen, then parameters must be selected that vary appropriately at the feature location. Once the parameters are chosen, first or second differences of each parameter are calculated to produce a set of raw weight functions. Next, the absolute value operator is applied to all values obtained. A normalization coefficient is then defined by

$$\alpha_k \equiv 1/\underset{k=1,m}{MAX}(\phi_k).$$

If the final weight function is to include dependence on more than one dependent variable a biasing coefficient γ_k can then be chosen to determine specific influence of each term in the linear combination. The partially processed weight function at each node is then described by

$$\omega = \sum_k \gamma_k \alpha_k |\phi_k| \tag{4}$$

This semi-raw weight function may contain values differing by many orders of magnitude. It also may contain very large spatial gradients which can result in unacceptable skewness or volume shear in the mesh. A procedure to limit the variation of the weight function which adjusts (somewhat) to the current distribution results from obtaining an average value of ω. The minimum value of ω is increased to a percentage of this average. All maxima greater than a chosen multiple of the average are truncated. The resulting distribution is then smoothed to reduce mesh skewness and shear.

In Step 4) the weight function (which can now be related to a source term in Poissons equation) obtained above is input to a modified Eiseman's mean-value relaxation algorithm. This can be determined for the computational cell in three dimensions by applying the following equation for each coordinate in turn:

$$\xi_{cm_{i,j,k}} = \frac{\sum_{k-1}^{k+1}\sum_{j-1}^{j+1}\sum_{i-1}^{i+1}\omega_{i,j,k}\xi_{i,j,k}}{\sum_{k-1}^{k+1}\sum_{j-1}^{j+1}\sum_{j-1}^{i+1}\omega_{i,j,k}} \tag{5}$$

This determines the movement of the mesh node at i, j, k to the center of mass for each stencil. This calculation is repeated for every point in the parametric domain except that a reduced stencil is used at boundaries. the mesh nodes are locally redistributed until a movement criteria is satisfied.

Once the new node positions are obtained in parametric space, the corresponding location in physical space is obtained from a simple mapping based on the initial transformation. No searches are required.

Implementation of Time Accurate Implicit Algorithm

An improvement on the long execution times of explicit flow solvers usually results when an implicit flow solver with a less severe CFL stability requirement is used. Unfortunately, most implicit algorithms are implemented in a non-time accurate manner for tractability and steady state convergence, and as a result, the implicit algorithms contain approximate factorizations, explicit boundary conditions, and linearization error, etc. The subiteration techniques of Pulliam (1993) can be used to restore time accuracy while still taking advantage of simplifying approximations to the implicit operator. Adding the time accurate subiterations to the existing implicit code of Edwards (1995a) would result in a time accurate upwind relaxation multigrid method. The implicit code as modified employs a second order LDFSS Edwards (1995b, 1997) upwind discretization

with optional FMG-FAS multigrid, uses a global constant time step subiteration and modifies the residual to enforce second order time accuracy when the subiterations converge. Also, the forward and backward relaxation parameters must be set to unity. A brief description of the implicit algorithm follows.

The subiteration techniques of Pulliam can be applied to the generic form of a system of partial differential equations. For development, consider the 2D Euler equations as written in strong conservation law form:

$$\frac{\partial U}{\partial t} + F(U) = 0 \tag{6}$$

where the non-linear flux vectors are

$$F(U) = \frac{\partial}{\partial x} E(U) + \frac{\partial}{\partial y} G(U). \tag{7}$$

An implicit approximation in time for the solution of equation (6) can be expressed as

$$\left[I + \frac{2\Delta t}{3} \frac{\partial}{\partial U} F(U^P) \right] \Delta U^P = -\frac{2\Delta t}{3} F(U^P) - \left[U^P - \frac{4}{3} U^n + \frac{1}{3} U^{n-1} \right] \tag{8}$$

Finally, divide by Δt_p, the physical time step, and multiply by 3/2.

$$\left[\frac{I}{\Delta t_p} + \frac{\partial}{\partial U} F(U^P) \right] \Delta U^P = - F(U^P) - \frac{\left[\frac{3}{2} U^P - 2U^n + \frac{1}{2} U^{n-1} \right]}{\Delta t_p} \tag{9}$$

Examining Equation (9) reveals the modifications required to the existing implicit code of Edwards to allow subiterating to a time accurate solution. For second order accuracy, the residual calculation must include the time difference. Storage must be provided for the extra time level required to calculate the second order time difference. A global physical time step must be specified for both the left and right hand side of the implicit solver. The modifications permit time accuracy to be achieved by subiterating the implicit flow solver.

Implementation of Adaptive Grid Algorithm in the Implicit Solver

If temporal accuracy is desired, it must be ensured while moving grid points. Two approaches have been tried: single equation and split equation. The split equation approach was

introduced by Benson and McRae (1992, 1993, 1989, 1990, 1991), continued by Laflin (1997) and is described in the proceeding section. The single equation approach was previously used in one dimension by Klopfer and McRae (1981) for explicit solvers and by Orkwis and McRae (1987) for implicit solvers. In the split equation approach, the grid adaption and solution update algorithms are completely independent of the flow solver algorithm. This permits integration of the governing equations on a stationary grid and does mesh point movement and solution update to the new grid independently of the flow solver. The split equation approach has the advantage of being extremely portable, but involves additional computation in the solution update calculation. To improve robustness and efficiency, a single equation implicit approach is taken to reduce the cost of solution update. The penalty paid for the single equation approach is a lack of portability. It is shown that the grid movement terms can be incorporated into any existing upwinding scheme which splits the inviscid flux into a convective and pressure contribution

This investigation builds on the previous work of Edwards (1995a) by implementing the time accurate subiterations of Rai (1987), modifying the algorithm to properly solve the unsteady transformation governing equations, and adding the parametric space point movement algorithm of Benson and McRae. Shock tube simulations were performed to ascertain the temporal accuracy of the algorithm for unsteady flow situations. The following section detail the modifications to the upwind relaxation multigrid algorithm of Edwards (1995a), and modifications to the Low-Diffusion Flux-Splitting of Edwards (1995b, 1997).

Incorporation of Grid Velocity in Upwinding

The flowfields under consideration are governed by the three dimensional compressible Navier-Stokes equations.

$$\frac{\partial U_1}{\partial t} + \frac{\partial E_1}{\partial x} + \frac{\partial F_1}{\partial y} + \frac{\partial G_1}{\partial z} = 0 \tag{10}$$

When a coordinate transformation is applied to Equation (10), an example contravariant velocity becomes

$$\hat{u} = \tilde{\xi}_x u + \tilde{\xi}_y v + \tilde{\xi}_z w \tag{11}$$

or

$$\hat{u}^{ut} = \tilde{\xi}_x u + \tilde{\xi}_y v + \tilde{\xi}_z w + \tilde{\xi}_t \tag{12}$$

depending on whether the transformation is for a steady or moving mesh system. The mesh velocity

$$\xi_t = -[x_\tau \xi_x + y_\tau \xi_y + z_\tau \xi_z] \tag{13}$$

illustrates how an example mesh speed appearing in the contravariant velocity. A simplification of this velocity reveals that the physical mesh velocity serves to correct the physical inertial velocity components for mesh movement.

$$\hat{u}^{ut} = \xi_x(u - x_\tau) + \tilde{\xi}_y(v - y_\tau) + \tilde{\xi}_z(\omega - z_\tau) \tag{14}$$

Now, consider the resulting unsteady transformation convective flux,

$$E^c ut = J \mid \nabla\xi \mid \rho[\tilde{\xi}_x(u - x_\tau) + \tilde{\xi}_y(v - y_\tau) + \tilde{\xi}_z(w - z_\tau)] \begin{bmatrix} 1 \\ u \\ v \\ w \\ H \end{bmatrix} = J \mid \nabla\xi \mid \left\{ \begin{bmatrix} \rho\hat{u} \\ \rho\hat{u}u \\ \rho\hat{u}v \\ \rho\hat{u}w \\ \rho\hat{u}H \end{bmatrix} + \begin{bmatrix} \rho\tilde{\xi}_t \\ \rho\tilde{\xi}_t u \\ \rho\tilde{\xi}_t v \\ \rho\tilde{\xi}_t w \\ \rho\tilde{\xi}_t H \end{bmatrix} \right\}. \tag{15}$$

With the exception of the energy term, the unsteady transformation convective flux calculated with $\hat{u}^{ut}$ achieves the desired goal of including the grid speed terms $(U\xi_t)$ in the original fixed mesh upwinding formulation. Comparing the energy term in Equation (11) to the desired term $(e_t\tilde{\xi}_t)$, one is energy while the other is enthalpy, thus they differ by a pressure term. To convert enthalpy to the desired energy term $(e_t\xi_t)$, a pressure term $(\rho\xi_t)$ must be subtracted from the energy term in the pressure component of the upwinding. The resulting unsteady transformation pressure flux is as follows:

$$E_{ut}^{p} = J \mid \nabla\xi \mid_{p} \begin{bmatrix} 0 \\ \tilde{\xi}_x \\ \tilde{\xi}_y \\ \tilde{\xi}_z \\ -\tilde{\xi}_t \end{bmatrix} = J \mid \nabla\xi \mid_{p} \begin{bmatrix} 0 \\ \tilde{\xi}_x \\ \tilde{\xi}_y \\ \tilde{\xi}_z \\ x_\tau\tilde{\xi}_x + y_\tau\tilde{\xi}_y + z_\tau\tilde{\xi}_z \end{bmatrix} \tag{16}$$

In summary, to incorporate the unsteady transformation grid speed terms into an existing upwinding, the only changes required are to use an unsteady transformation contravariant velocity (Equation 10) and an unsteady transformation pressure flux (Equation 16). The grid velocity is thereby included in the upwinding of the Low-Diffusion Flux-Splitting Scheme (LDFSS) of Edwards (1997).

Results

Computational results were obtained for a 2-D mixed compression inlet Neaves (1995a,b) (used as a code development case), for a swept sidewall inlet case, and for a 3-D hydrocarbon-fuel inlet-isolator-diffuser configuration designed and tested at NASA Langley Research Center in the M4BDF Emami (1995). The swept sidewall compression inlet results obtained were very preliminary and were reported in the first progress report. This case was not continued due to lack of unrestricted data and post isolator geometry.

In order to reduce the number of issues while developing further the code, an axisymmetric inlet designed initially for the original SST program was chosen. The choice was influenced by the possibility of publishable data for this configuration, but the data remain restricted and were not included in this or other exposure of the work. The case did prove to be valuable for code development, so an example of the results obtained for free stream perturbation is included herein and other results are referenced.

The case that was used primarily for 3-D code development and comparison with experiment was a configuration chosen in consultation with Carl Trexler and Aaron Auslender of the Hypersonic Airbreathing Propulsion Branch, NASA Langley Research Center. The geometry was selected from a series of hydrocarbon fuel configurations tested in the Mach 4 Blowdown

Facility at Langley. The facility capabilities and results for a selection of the configurations appear in Emami, et al. (1995). The remainder of this section will give a brief description of the 2-D results for freestream perturbations and will present the results obtained for the 3-D Langley inlet.

Axisymmetric Mixed Compression Inlet

At the completion of the previous grant, some problems still remained which required resolution prior to proceeding with the 3-D hypersonic inlet computations. Initial resolution of these problems was conducted using a realistic axisymmetric inlet (Neaves (1995a,b).

The axisymmetric inlet geometry selected was that designed for the GE SST engine at cruise conditions. The geometry shown with minimal dimensioning appears in Figure 1. The forebody cone angle is 10.3°. The cowl begins 1.98 cowl lip radii from the centerbody tip and the design throat is located 1.86 cowl lip radii further downstream. The design bleed ports have been functionally grouped into five porous bleed regions located in the walls of the inlet to aid in stabilization at the critical operating condition. The cowl has two bleed regions with the remaining three on the centerbody. The first bleed regions on the centerbody and cowl (BP-1 and BP-4) are required to control the shock wave-boundary layer interaction. The throat bleed regions (BP-2 and BP-5) are needed to stabilize the terminating normal shock wave. The diffuser bleed region (BP-3) is required to minimize separation. The mass flux as given in Table 1 represents 6.0% of the captured mass flow.

Table 1: Bleed regions

Bleed region	Location	x/r_{cowl}	Percentage of mass flow
BP-1	Centerbody	3.40 - 3.70	1.0
BP-2	Centerbody	3.80 - 4.15	1.5
BP-3	Centerbody	4.20 - 5.10	1.0
BP-4	Cowl	3.20 - 3.60	1.0
BP-5	Cowl	3.75-4.15	1.5

Prior to unstart simulations, critical flow was established in the inlet at design flight conditions, 60,000 ft (18,288m) at a freestream Mach number of 2.35. The inlet design normal shock Mach number is 1.3 at a location 0.12 radii aft of the throat. The initial grid from GRIDGEN2D was slightly preclustered to the boundary layer and contains 8100 points. The terminating normal shock wave was stabilized near the aft region of the throat bleed bands about 0.3 radii downstream of the throat. The back pressure required for this shock location is $11.7P_\infty$ which represents about 85% total pressure recovery. The shock location was further aft than the inviscid design location due to an inability to stabilize the normal shock near the design location with any bleed rate. At the design shock location, the normal shock was apparently destabilized by a midpoint intersection with a reflected shock. The shock will not stabilize aft of the critical condition due to viscous boundary layer interactions. Small separation regions exist downstream on the centerbody and cowl at the critical operating condition due to the large diffuser area ratio. The adapted grid resolves the shock waves and boundary layers ($\hat{n}^+ \leq 7$, for the first grid cell), and adapts to the train of weak reflections of the cowl shock wave.

Results were obtained for two types of perturbations to the critical inlet flowfield: sub-critical, i.e., too weak to cause an unstart; and super-critical, i.e., severe enough to cause an unstart. The perturbations considered were finite-rate changes of freestream temperature and compressor face pressure. The temperature perturbation changes freestream pressure while holding density and velocity constant, thereby varying freestream Mach number. All perturbations are initiated over a real time of 5 milliseconds which corresponds to a non-dimensional time of $4.08t_C$.

A full description of the computational results obtained for both temperature and downstream pressure perturbations appears in Neaves and McRae (1995a) and Neaves (1995b). For illustrative purposes, computational results for a 10% freestream temperature increase ramped linearly over 5ms are shown in Figure 2.

At 5ms (frame 1 of Figure 2), the freestream temperature ramped increase is complete. The end of the transient is a vertical contour in front of the centerbody cone due to the lowering effect

on Mach number. The curved contour in the conical shock is caused by the faster propagation of the ramping transient outside of the conical shock. The lower Mach numbers cause increased shock angles. The resulting stronger shocks then cause the normal shock to begin moving toward the throat to match exit pressure (10.14ms). The increased strength of the reflected shocks is evident in the adapted grid where more points are used to resolve the shocks. At 14.86ms, the normal shock is still moving forward, and a normal shock has formed on the centerbody at the base of a reflection. The throat Mach number has fallen below one, and by 19.14ms a normal shock has formed forward of the throat, and the aft normal shock is dissipating. As the forward normal shock moves upstream of the bleed regions, the flow separates and lambda shocks form (23.32ms and 27.50ms). The lambda structure continues forward, and by 31.68ms a normal shock has formed as the area increases. The unstart requires 36.09ms to reach the cowl lip.

As can be seen in Figure 2, the adapted grid increased resolution such that inference of cause and effect was possible as the shock/separation system initiated and propagated forward. At this juncture, the 3-D inlet computations were begun.

Dual-Mode Scramjet Inlet-Isolator-Diffuser

As noted previously, a 3-D inlet case was chosen for computation for which unrestricted data were available, through the kind cooperation of the Hypersonic Airbreathing Propulsion Branch, NASA Langley Research Center. The computational conditions were chosen to match the nominal test conditions for the M4BDF (Emami, et al. (1995)).

$M_\infty = 4.03$
$P_{0\infty} = 200$ psia
$P_\infty = 1.266$ psia
$Re_X = 21 \times 10^6$/ft

Standard temperature was used as the total temperature for computation, since the tunnel is unheated and tunnel flow temperature typically varied between 500°R and 540°R.

The geometry (Emami, et al. (1995)), including actuated surfaces and instrumentation locations, for the computed dual-mode scramjet configuration shown in Figure 3. The geometry shown is one of a series of configurations used to produce experimentally a parametric data base

for evaluating the performance of inlet/isolator combinations. The overall goal of this study was to produce data for use in a cycle deck to predict inlet-isolator performance over the ramjet/envelope for use in design.

The purpose of the isolator is, as it's name implies, is to isolate the combustor from the inlet in order that the shock system at the burner entrance does not produce an unstart during ramjet operation. The isolator provides a substitute for the boundary-layer bleed used to stabilize the shock system in the SST type mixed compression inlet of the previous section. Boundary-layer bleed is increasingly impractical as stagnation temperature increases with Mach number.

The design goal is to determine the shortest isolator that will permit the maximum practical combustor pressure rise without unstart. For long isolators, 90% of the normal shock pressure rise at the throat seems possible. However, the structural weight of such designs is prohibitive. The study by Emami, et al. (1995) examines selected isolator lengths and other configuration variations by using a flow metering device to slowly increase the pressure in the combustor section until the inlet unstarts. The maximum pressure obtained prior to unstart becomes a figure-of-merit for the configuration. However, computational results obtained as part of the present study indicate that conclusions drawn from this experimental study may only be applicable to quasi steady operation. When unsteady effects are included, the stability margin may be reduced.

Code Modifications and Problem Resolution

Initial results obtained with the explicit code revealed that the Langley geometry would provide a severe test for DSAGA. The geometry-preserving changes developed during the axisymmetric inlet work had to be implemented in 3-D, which proved to be a demanding task. Another problem is that when the plenum and throttling device is included in the computation, the aspect ration of the computational domain becomes very large. This tends to require large mesh node movement as the solution evolves, which severely taxes the 3-D adaptive algorithm.

The 3-D investigation with the explicit version of DSAGA was characterized by frequent unstable flow solver/adapter interaction. The following actions were taken to remove the unstable behavior:

1) Unstable Turbulence Model Interaction. The one-equation Baldwin and Barth Turbulence Model caused instability near viscous boundaries when starting adaption. This interaction occurs at yet unresolved viscous boundaries where the mesh has not clustered sufficiently to resolve the relevant length scales for the turbulence model. Preclustering and/or using the adaption to resolve the boundary layers prior to general flowfield adaption removed the unstable interaction.
2) Parametric Space Solution Update. The 3-D adapter previously proved to be unstable near discontinuous surface slope changes in 3-D due to the temporary loss of geometry as mesh points moved through the slope change. The loss of geometry occurs when a surface mesh line does not coincide with the line of discontinuous surface slope. In a fixed grid calculation, the only result of this situation is a local change in the apparent geometry of the surface. However, for moving meshes, the surface grid points are constrained to move in the known geometry surface, implying that there can be no contribution to cell volume change from this movement. The standard volume calculation procedure used in physical space to determine changes in cell volume due to mesh movement will, however, result in erroneous calculations of cell volumes at the boundaries. These erroneous volumes add sources/sinks to the conservative variable update. An efficient alternative appeared to be performing the update in the same parametric space used to move the points thereby eliminating boundary discontinuities. The parametric space volume calculation requires the same number of floating point operations, and update sweep volumes next to boundaries are always zero.

   The parametric space update worked well in the adaption algorithm, but when coupled with a physical space flow solver, global conservation was violated. The slight errors between volume calculations in parametric space and physical space seemed to generate sinks and sources. The lack of global conservation resulted in an unstable flow solver and adapter interaction.

Several approaches were implemented in search of stabilizing the flow solver/adapter interaction. A more accurate volume calculation algorithm using the techniques of Kordulla and Vinokur (1983) was implemented. Various volume calculations were considered in the flow solver and the adapter with no significant improvements. Since the unstable interaction does not appear to be caused by inaccurate volume calculations, a reasonable culprit might be the remapping inaccuracies occurring when remapping from parametric to physical space. The accuracy of the transformation from parametric to physical space was increased by one order (Laflin (1997)). The increased accuracy is obtained by retaining four more terms of the Taylor Series expansion for a total of seven terms. The higher order remapping did not solve the unstable interaction problem. Additionally, an upwinding scheme adapter was added in solution update step (Laflin (1997)) which upwinds the solution variables based upon the direction of cell wall movement. As a last resort, a non-conservative limiter was included in the adapter solution update algorithm to prevent new maxima and minima

Unfortunately, none of these actions were entirely successful, so work was initiated to modify the code of Edwards (1997) for time dependency and to install the adaptor.

Inviscid Adapted Grid Results

Prior to the unstable interaction, the inviscid version of DSAGA produced reasonably well resolved pre-unstart solutions for the M4BDF case. Figures 4 and 5 illustrate a centerline plot of the adapted computational grid and computed Mach contours for a value of the flow meter exit height of $H_{fm} = 0.92$ in. As is evident from Figure 4, adaptation is quite reasonable for the wedge and cowl shock waves. Adaptation is less adequate for the isolator, but is sufficient to allow analysis of the isolator flow for the Baldwin Barth turbulence model.

Examination of the Figure 4 and 5 Mach contours in the isolator section reveals that the expected (Emami (1995)) "Normal Shock Train" does not occur in this case. Instead, diffusion occurs through a series of reflected oblique shock waves originating from the cowl shock. A more

accurate description would be an "oblique shock train". More analysis will be provided below when compared with experiment.

The flow was initiated impulsively for this case, resulting in very chaotic flow in the flow metering section. Note that the Mach number varies greatly in this section due to the channel spanning vortices, etc.

Implicit Unadapted Grid Results

After installing the subiteration routines in the existing Implicit code of Edwards (1997), an M4BDF case computation was performed prior to installing the adaptive grid routines. Conditions were chosen (H_{fm} = 0.3 in.) such that the normal shock system should have stabilized just at the entrance of the isolator (Figure 11). Results from this run are shown as Mach contour plots in Figure 6.

The sequence begins with the top left plot in Figure 6, in which the shock system is nearing the isolator. The shock system then enters the isolator (left column sequence) and rather than stabilizing at the isolator entrance, continues forward for a full unstart (right column sequence).

Implicit Adapted Grid Results

After completing this run, the adapter was installed in the implicit algorithm as a modification to the transformed convective velocity in the governing equations. As described previously, the integration and adaption is performed as a single implicit step (with inner iterations) rather than as two explicit steps.

A solution for the conditions of Figure 6 is shown in Figure 7 prior to entry of the moving shock system into isolator. Note that the adapter resolves the wedge shock wave well but does not exhibit the same degree of adaptation to the other features as found in the explicit code. This is, in part, due to the need for adjusting the adaptive weight function for the implicit code and a different turbulence model. It is obvious immediately that the Spalast-Almaras turbulence model carried over from Edward's implicit code results in thicker viscous layers than the Baldwin-Barth model in the explicit code (compare Figures 4 and 7). This also changes the flow features in the isolator,

although a definitive examination will require more adaptation. In any case, neither code predicts a normal shock train in the isolator.

The flow structure characteristics needed to instigate the shock train in the isolator can be deduced from the mixed compression inlet plots of Figure 2. In this case the cowl shock wave initiates a similar series of cowl shock reflections. However, the lower freestream Mach number and the area reduction reduce local Mach number until a new normal shock is formed at the throat. This shock separates the flow at both walls, resulting in an unstable (due to increasing upstream area) system which propagates forward rather than stabilizing or initiating a "train". It is interesting to note that the shock system does have the configuration usually found in a "normal shock train" as it exits the inlet.

For the conditions of the M4BDF case, no normal shock train system was observed in the computational study. Given the combination of asymmetric compression surfaces, isolator aspect ratio, and Reynolds number for this case, it is unlikely that a conventional normal shock train will occur in the isolator unless it occurs only as a result of accurate combustion simulation.

Figure 8 gives a typical cross section of the flow in the isolator for this case. The cross flow Mach contours shown on the surface (not planar, due to adaptation) show the effect of the corner vortices resulting from the wedge/sidewall interaction.

Figure 9 shows a comparison of lower surface centerline pressure through the isolator for the explicit adapted solution (Figures 4 and 5) and the implicit unadapted solution prior to unstart (Figure 6). This plot confirms that the boundary layer produced by the turbulence model in the explicit code is too thin as evidenced by the cowl shock intersecting the wedge downstream of the experimental location (i.e., the displacement thickness is reduced on both compression surfaces). However, the explicit code solution trends are correct downstream of the first pressure increase, except for a tendency to over expand prior to separation reattachment. The implicit unadapted solution exhibits the correct cowl shock/ lower surface intersection location, indicating that turbulence model is producing a more accurate displacement thickness. However, the flow in the

isolator is clearly underresolved and it is also likely that the separations are more extensive than in the experiment.

As noted previously, the implicit unadapted case unstarted rather than stabilizing. Figure 10 shows the pressure distribution through the entire inlet/flow meter as the computational shock system is translating through the position at which the experimental shock system is stable. The most likely explanation for this behavior is that the turbulence model does not model separations correctly, thereby producing a shock wave induced separation extensive enough to extend past the beginning of the isolator into the converging section of the inlet. A second possibility is that, since the computation was initiated from the prior condition impulsively, unsteady effects caused the shock to continue movement. Figure 11, supplied by C. Trexler, illustrates the runs made for this isolator length/cowl angle combination. Shock systems in the isolator were found to be stable for experimental flow meter exit heights between 0.34 inches and 0.70 inches.

Interactions

Mr. Carl Trexler and co-workers of the Hypersonic Airbreathing Propulsion Branch at NASA Langley have expressed interest in our inlet research and have helpfully provided data and geometries for use in our calculations.

Carl A. Trexler
Phone: 757-864-6247
Mail Stop 168
12 Langley Boulevard
NASA Langley Research Center
Hampton, VA 23681-0001

Aaron Auslender
Phone: 757-864-6545
Mail Stop 168
12 Langley Boulevard
NASA Langley Research Center
Hampton, VA 23681-0001

Many helpful discussions concerning inlet characteristics and computational boundary conditions have been conducted with

Dr. Gerald (Jerry) C. Paynter
Phone: 206-655-4948
Boeing Commercial Aircraft Co.,
Mail Stop 49-53
P. O. Box 3707
Seattle, WA 98124

Conclusions

Work under AFOSR grant F49620-94-1-0237 has been completed. Dynamic Analysis of two inlet configurations was reported, the first of which was an axisymmetric mixed compression inlet used for code development and the second was a generic hydrocarbon fuel dual-mode scramjet inlet-isolator-diffuser configuration tested in the M4BDF at NASA Langley.

Evaluation of the axisymmetric mixed compression inlet results led to observations and conclusions:

1) The terminating normal shock could not be stabilized at the inviscid design location, regardless of the magnitude of boundary layer bleed. This points to the need for inclusion of viscous effects in the design process.

2) Unstart of the inlet at design conditions could be induced by a 10% freestream temperature perturbation or a 5% change in diffuser/compressor face pressure. This indicates clearly that dynamic analyses of all inlet designs should be conducted before they are finalized.

3) The use of the dynamic adaptive grid algorithm resulted in well resolved simulations for this case and allowed assessment of cause and effect and a full analysis of the unstart sequence for all conditions.

The dual mode scramjet inlet-isolator-diffuser configuration proved to be a demanding case for the adaptive mesh algorithm, thereby requiring modification of the algorithm and transition to an implicit code. The 3-D explicit version of the code provided solutions for the flow through the isolator section that exhibited an oblique shock train rather than the normal shock train expected for ramjet operations. Dynamic instabilities occurred in this code which precluded a full unstart calculation.

The new 3-D implicit code, after modification for time accuracy, was used to simulate the approach dynamically of conditions which, in experiment, resulted in a stable shock system at the isolator entrance when the shock system was moved upstream gradually. In the fixed mesh computational simulation, the shock system continued upstream and unstarted the inlet rather than attaining a stable location. This run was compared with results from the explicit adaptive code and

experiment, for steady flow in the isolator section. Obvious differences due to turbulence modeling were observed, with the explicit code producing obviously thin viscous layers and the implicit code producing thick boundary layers. Although the fixed mesh 3-D implicit code produced much thicker viscous layer/separations in the isolation, an oblique shock reflection system was still present in the isolator, rather that a normal shock train. A comparison of lower wall pressure distribution with experiment as the stable location showed good agreement except in the diffuser.

The adaptive mesh implicit code proved to be more efficient and robust, however some instabilities were still encountered. As development of this version of the code continues, it is anticipated that calendar time for analysis of an inlet will be much reduced.

The results of the 3-D dual-mode scramjet runs lead to the following conclusions:

1) The diffusion in the isolator (prior to combustor shock simulation) results from a oblique shock system. No indication of a normal shock train was found.

2) Dynamic effects, a less than accurate turbulence model, and an unresolved mesh must be considered as possible causes of the fixed mesh computational unstart encountered for quasi-stable experimental conditions. Further investigation is needed to assess the degree to which these possible causes contributed. Results obtained to date with the adapted implicit codes are promising.

3) It is clear that dynamic experimental data will be required to verify fully the computational results.

Publications

Masters Thesis:

Neaves, M. D. 1995. "Numerical Investigation of the Unstart Phenomenon in an Axisymmetric Supersonic Inlet," Masters Thesis, Mechanical and Aerospace Engineering, North Carolina State University, Raleigh, NC.

Proceedings:

Neaves, M. D. and McRae, D. S., "Numerical Investigation of the Unstart Phenomena in an Axisymmetric Supersonic Inlet," Proceedings, International Symposium on Computational Fluid Dynamics in Aero Propulsion, ASME International Congress and Exposition, San Francisco, CA, Nov. 12-17, 1995, pp. 149-156.

Neaves, M. and McRae, D. S., "Numerical Investigations of Axisymmetric and Three-Dimensional Supersonic Inlet Flows using a Solution Adaptive Mesh," Proceedings, First AFOSR Conference on Dynamic Motion CFD, Rutgers Univ., NJ, June 2-5, 1996, pp. 235-244.

Future Research

Two directions are suggested for future research in the dynamic computational analysis of scramjet configurations, both based on further development of the time-accurate implicit code detailed in this report:

1) The results of this research demonstrate that the dynamic analysis of scramjet configurations must include a detailed dynamic simulation of combustion in order to conduct the analyses that will most assist the design process. The difficulty and expense of hypersonic propulsion module testing is prohibitive, and the capability to add dynamics, with temporally resolved data collection, does not exist to any reasonable extent. The computational approach, however, shows promise for allowing analysis of full modules.

2) The results presented for unstarts were halted when the shock system reached the inlet cowl lip. However, in a complete aircraft configuration, the shock system will exit the inlet and couple with the outer flow and structure of the aircraft. In the case of closely coupled inlet modules, the flow downstream of the shock system could be ingested by the adjacent inlet and initiate chained unstart. Also inlet buzz could be initiated, resulting high dynamic loading of the module structure. Dynamic computational analysis of external coupling of the unstart is within the capability of the present code, with modifications.

Pacing Item

The primary pacing item for both of the suggested directions is the paucity of temporally resolved data for high speed inlet and propulsion modules. It is strongly urged that a research effort be initiated to obtain useful, unrestricted dynamic inlet data. An initial collaboration with NASA Langley for testing, at M=6, an inlet designed jointly (with NCSU) was halted in model construction by lack of NASA internal funding. If the numerical techniques are to be verified to the extent that they will be useful to the design process, dynamic data are essential.

References

Benson, T. J. 1986. "Three-Dimensional Viscous Calculation of a Flow in a Mach 5.0 Hypersonic Inlet," AIAA Paper 86-1461.

Benson, R. A. 1989. "A Dynamic Solution-Adaptive Grid Algorithm in Two and Three Dimensions," Masters' Thesis, North Carolina State University, Raleigh, NC.

Benson, R. and McRae, D. S. 1990. "A Three-Dimensional Dynamic Solution Adaptive Mesh Algorithm", AIAA 90-1566, AIAA 21st Fluid, Plasma Dynamics, and Lasers Conference, Seattle, WA.

Benson, R. and McRae, D. S. 1991. "A Solution Adaptive Mesh Algorithm for Dynamic/Static Refinement of Two and Three Dimensional Grids", Third International Conference on Numerical Grid Generation in Computational Fluid Dynamics and Related Fields, Barcelona, Spain.

Benson, R. A. and McRae, D. S. 1992. "Numerical-Simulations Using a Dynamic Solution-Adaptive Grid Algorithm, with Applications to Unsteady Internal Flows," AIAA 92-2719, 10th Applied Aerodynamics Conference, Palo Alto, C.

Benson, R. A. and McRae, D. S. 1993. "Numerical Simulations of the Unstart Phenomena in a Supersonic Inlet/Diffuser," AIAA 93-2239, 29th AIAA/SAE/ASME/ASEE Joint Propulsion Conference, Monterey, CA.

Edwards, J. R. 1995a. "Development of an Upwind Relaxation Multigrid Method for Computing Three-Dimensional Viscous Internal Flows," *AIAA Journal of Propulsion and Power*, Vol. 12, No. 1, pp. 146-154

Edwards, J. R. 1995b. "A Low-Diffusion Flux-Splitting Scheme for Navier-Stokes Calculations," AIAA Paper 15-1703CP.

Edwards, J. R. 1997. "A Low-Diffusion Flux-Splitting Scheme for Navier-Stokes Calculations," *Computers and Fluids*, Vol. 26, No. 6, PP. 635-659.

Emami, S., Trexler, C. A., Auslender, A. H., and Weidner, J. P. 1995. "Experimental Investigation of Inlet-Combustor Isolators for a Dual-Mode Scramjet at a Mach Number of 4," NASA Technical Paper 3502.

Holland, S. D. 1991. "A Computational and Experimental Investigation of a Three-Dimensional Hypersonic Scramjet Inlet Flow Field," Ph.D. Dissertation, North Carolina State University, Raleigh, NC.

Kerrebrock, J. L. 1992. "Some Readily Quantifiable Aspects of Scramjet Engine Performance," *AIAA Journal of Propulsion and Power*, Vol. 8, No. 5, pp. 1116-1122.

Klopfer and McRae, D. S. 1981. "The Nonlinear Modified Equation Approach to Analyzing Finite Difference Schemes," AIAA 81-1029, 5th AIAA Computational Fluid Dynamics Conference, Palo Alto, CA, 1981.

Kordulla, W. and Vinokur, M. 1983. "Efficient Computation of Volume in Flow Predictions," *AIAA Journal*, Vol. 21, No. 6, p. 917.

Laflin, K. R. 1997. "Solver-Independent *r*-Refinement Adaption for Dynamic Numerical Simulations," Ph.D. Dissertation, North Carolina State University, Raleigh, NC.

Neaves, M. D. 1995. "Numerical Investigation of the Unstart Phenomenon in an Axisymmetric Supersonic Inlet," Masters Thesis, Mechanical and Aerospace Engineering, North Carolina State University, Raleigh, NC.

Neaves, M. D. and McRae, D. S. 1995. "Numerical Investigation of the Unstart Phenomenon in an Axisymmetric Supersonic Inlet," Proceedings, International Symposium on Computational Fluid Dynamics in Aeropropulsion, AD-Vol. 49, ASME, San Francisco, CA, pp. 149-156.

Orkwis, P. D. and McRae, D. S. 1987. "Analysis of Standard Implicit Schemes with Arbitrary Mesh Movement," AIAA 87-1171, AIAA 8th Computational Fluid Dynamics Conference, Honolulu, Hawaii.

Pulliam, T. H. 1993. "Time Accuracy and the Use of Implicit Methods," AIAA Paper 93-336.

Rai, M. M. 1987. "Navier-Stokes Simulations of Blade-Vortex Interaction Using High-Order Accurate Upwind Schemes," AIAA Paper No. 87-0543.

Singh, D. J., Trexler, C. A., and Hudgens, J. A. 1992. "Three-Dimensional Simulation of a Translating Strut Inlet," AIAA Paper 92-0270.

Weir, L. J., D. R., and Rupp, G. D. 1989. "Mach 5 Inlet CFD and Experimental Results," AIAA Paper 89-2355.

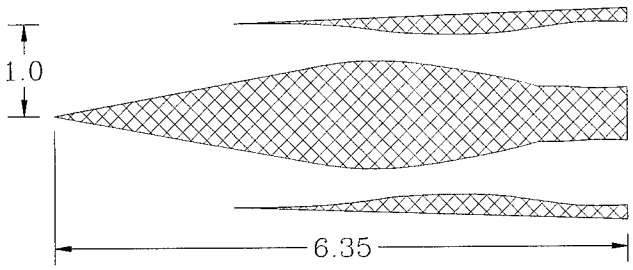

FIGURE 1: AXISYMMETRIC INLET GEOMETRY

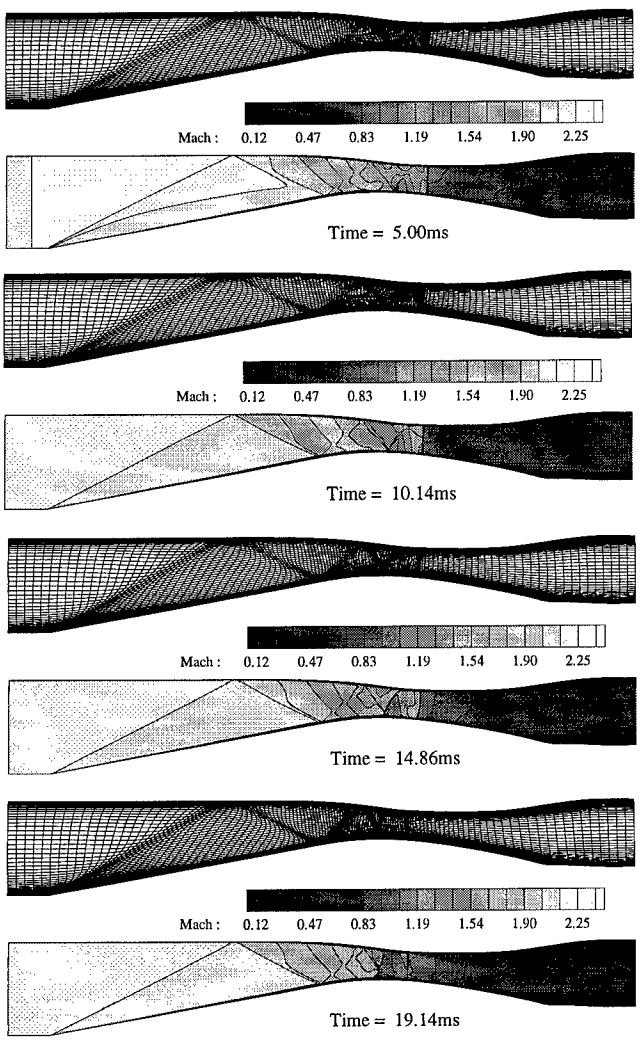

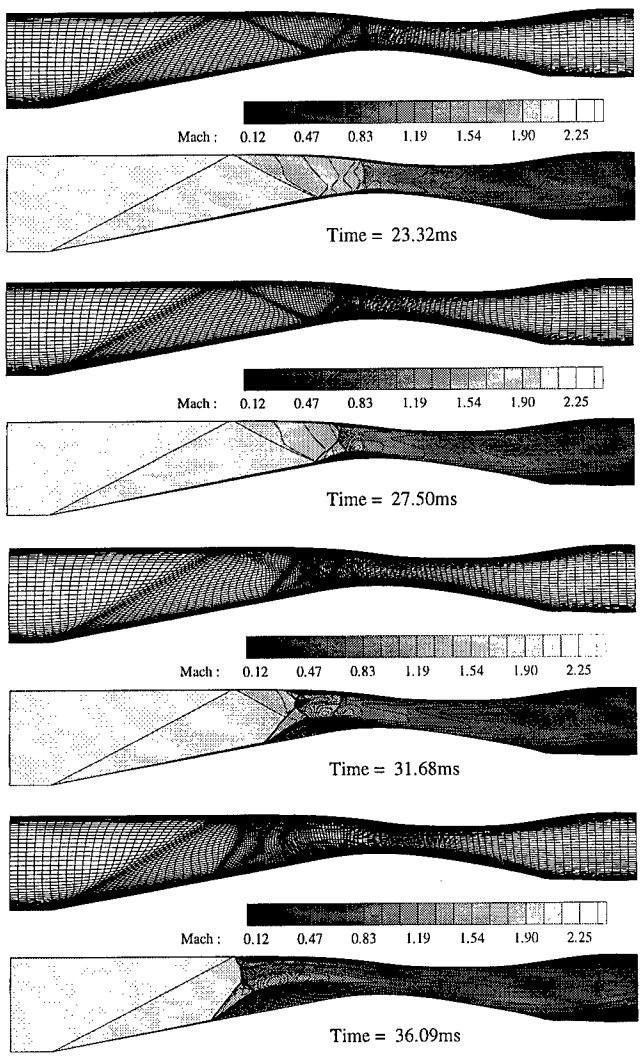

FIGURE 2: SUPER-CRITICAL TEMPERATURE INCREASE

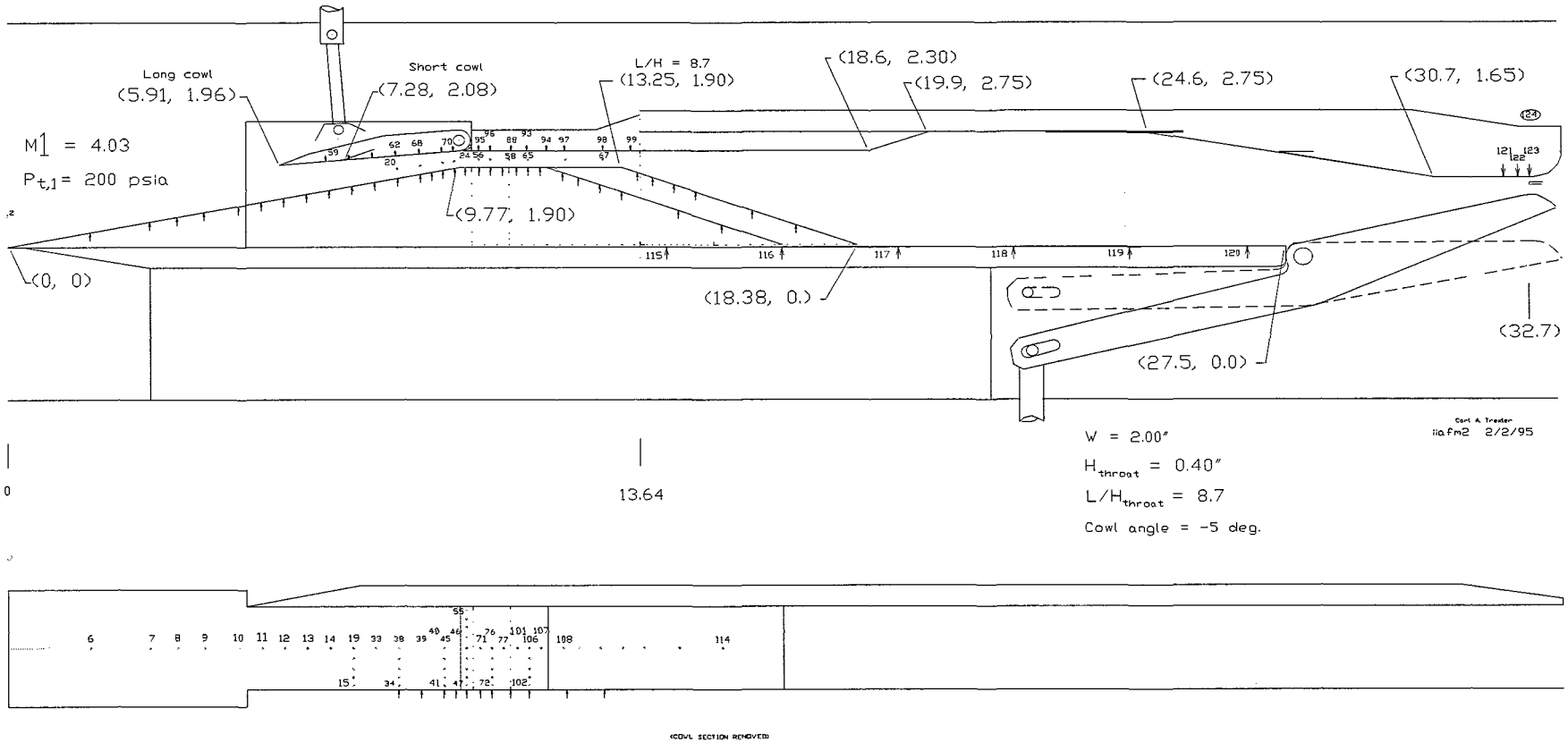

FIGURE 3: DUAL-MODE SCRAMJET INLET MODEL

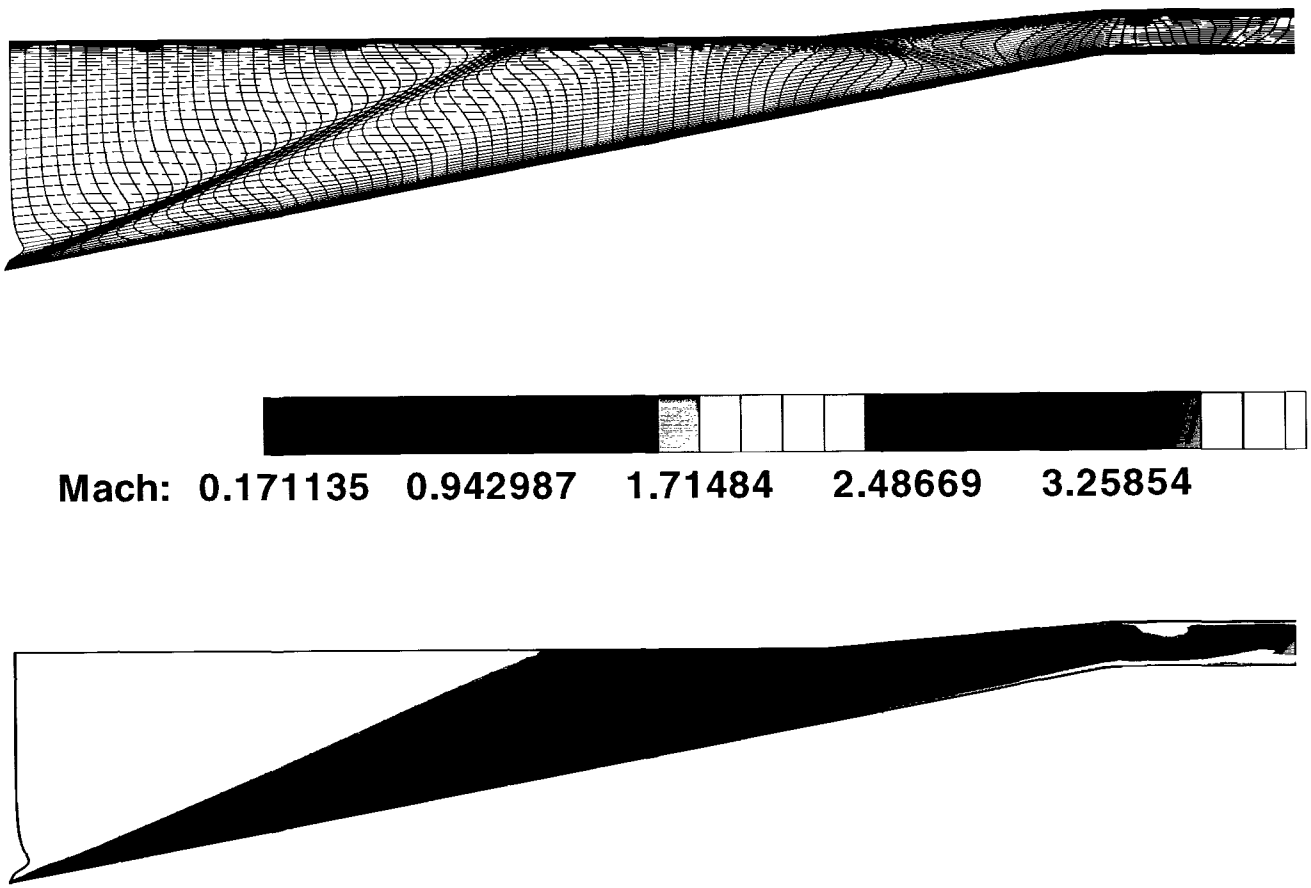

Figure 4: Adapted Explicit: Scramjet Inlet Adapted Grid and Mach Contours

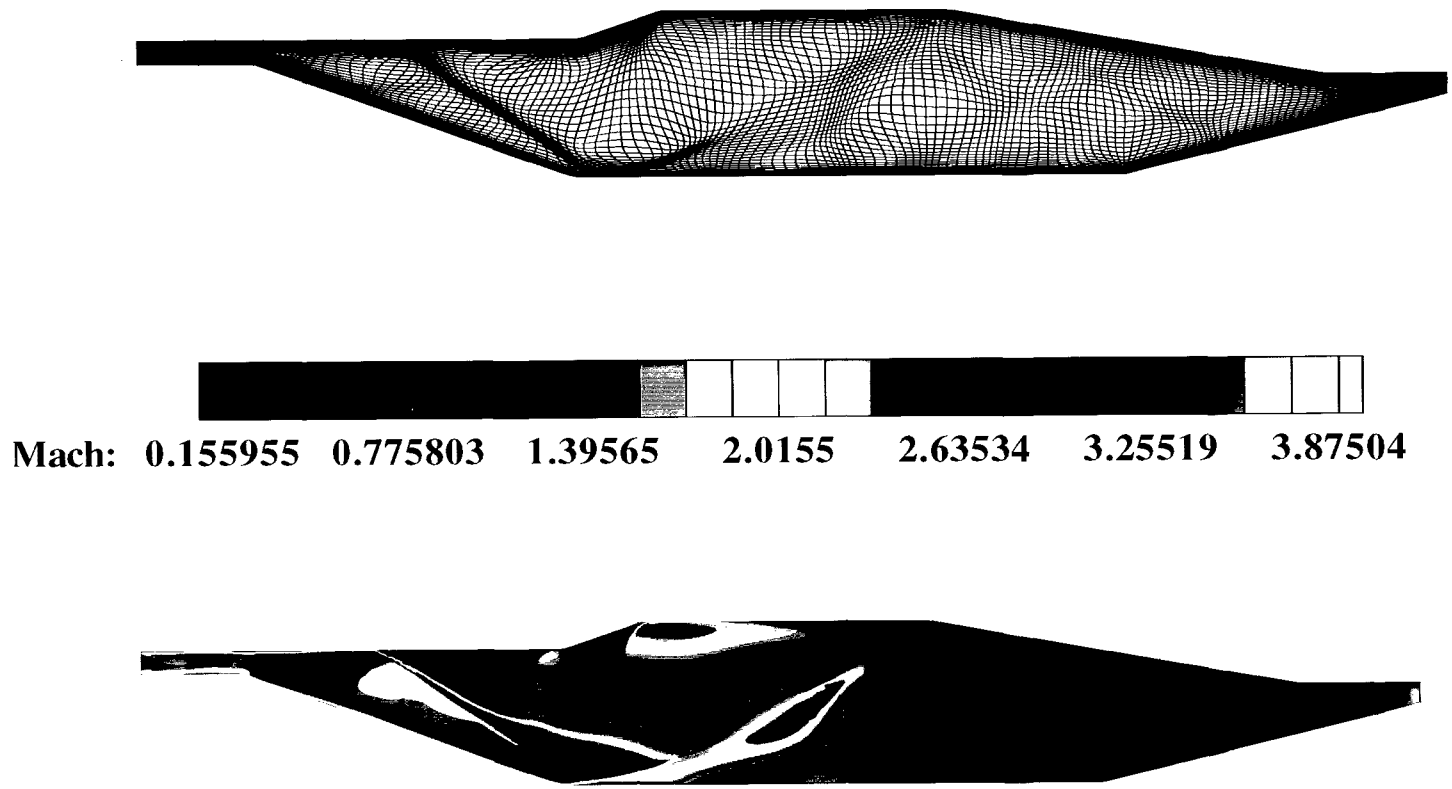

Figure 5: Adapted Explicit: Scramjet Diffuser Grid and Mach Contours

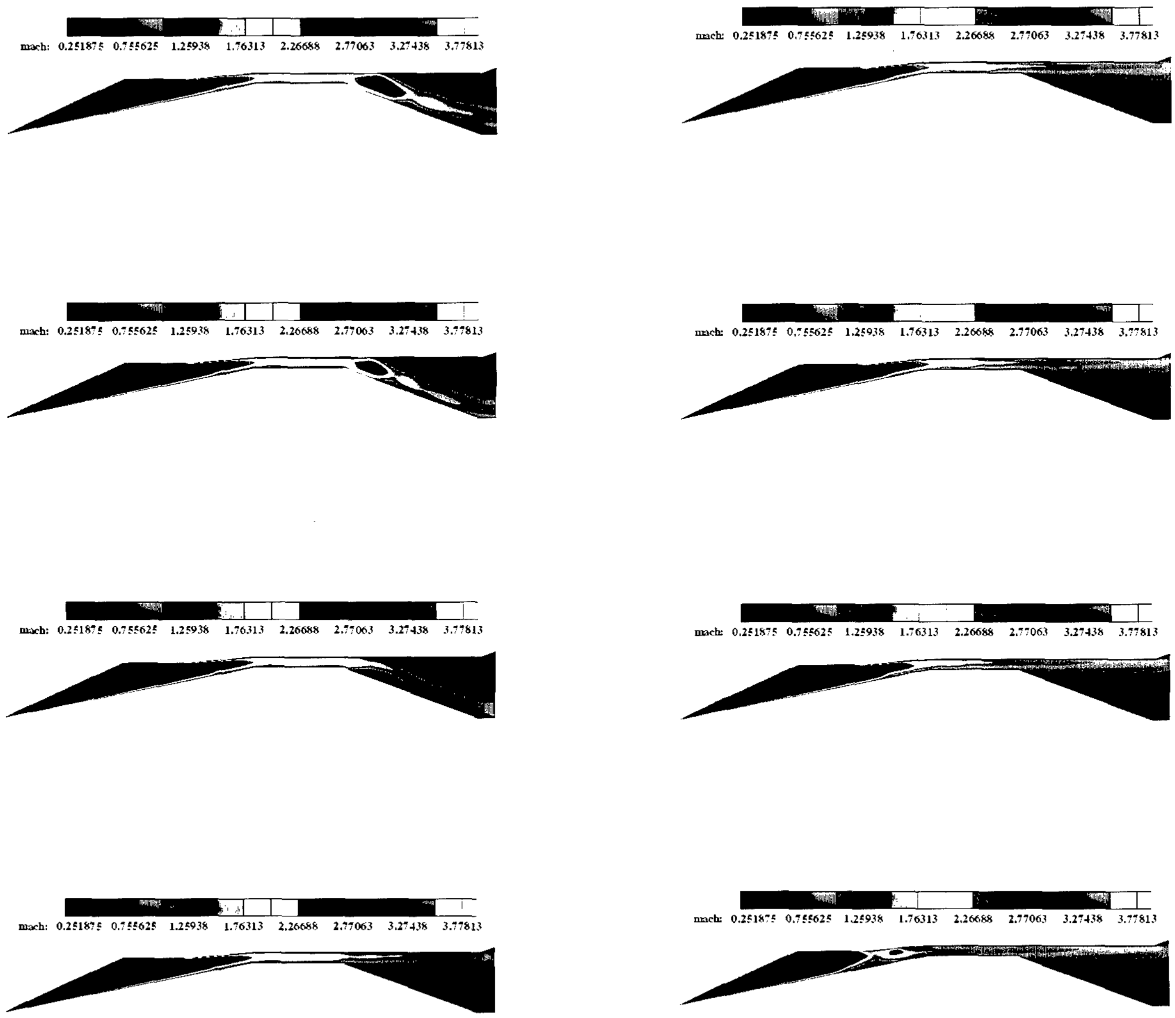

FIGURE 6: UNADAPTED IMPLICIT UNSTART SEQUENCE

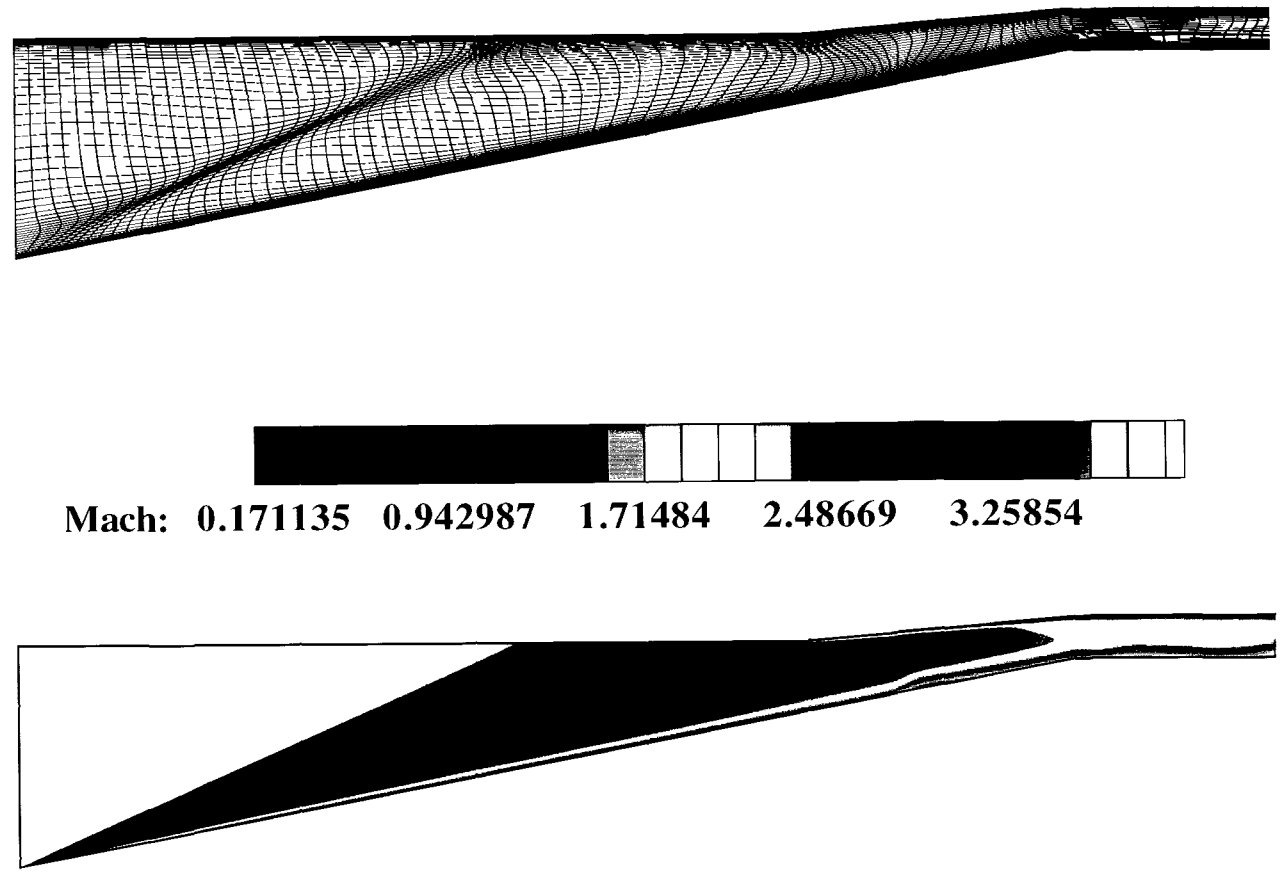

Figure 7: Adapted Implicit: Scramjet Inlet Adapted Grid and Mach Contours

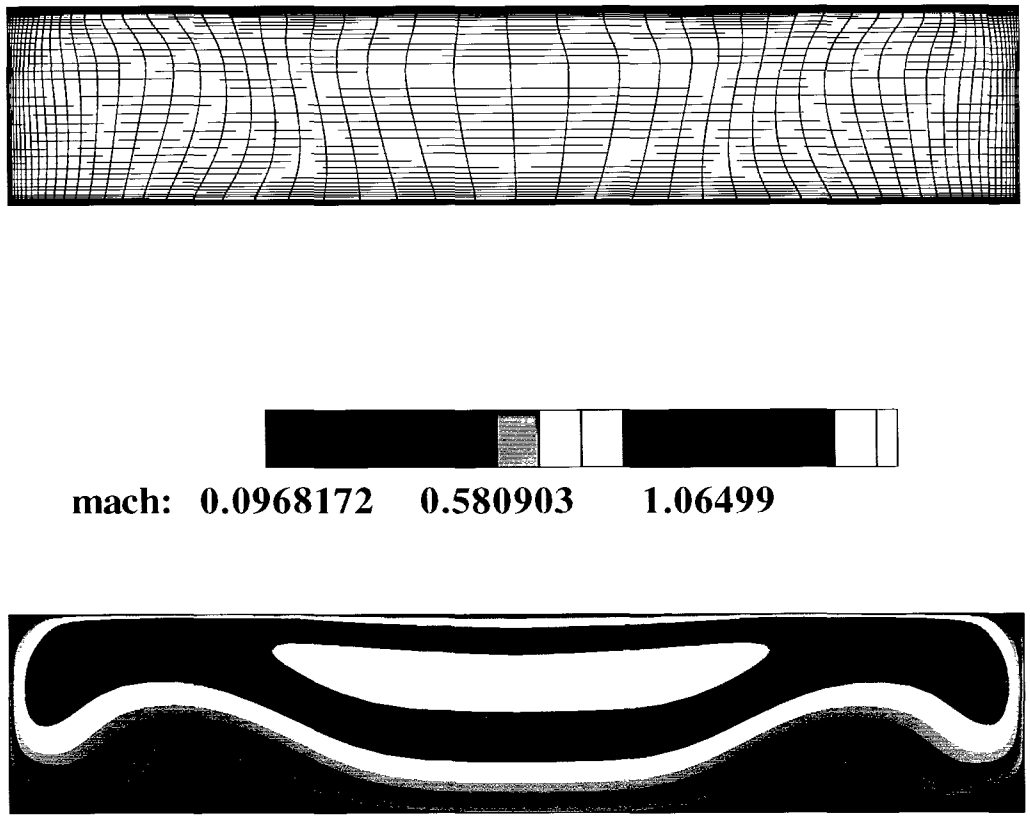

Figure 8: Adapted Implicit: Isolator Crossflow Grid and Mach Contours

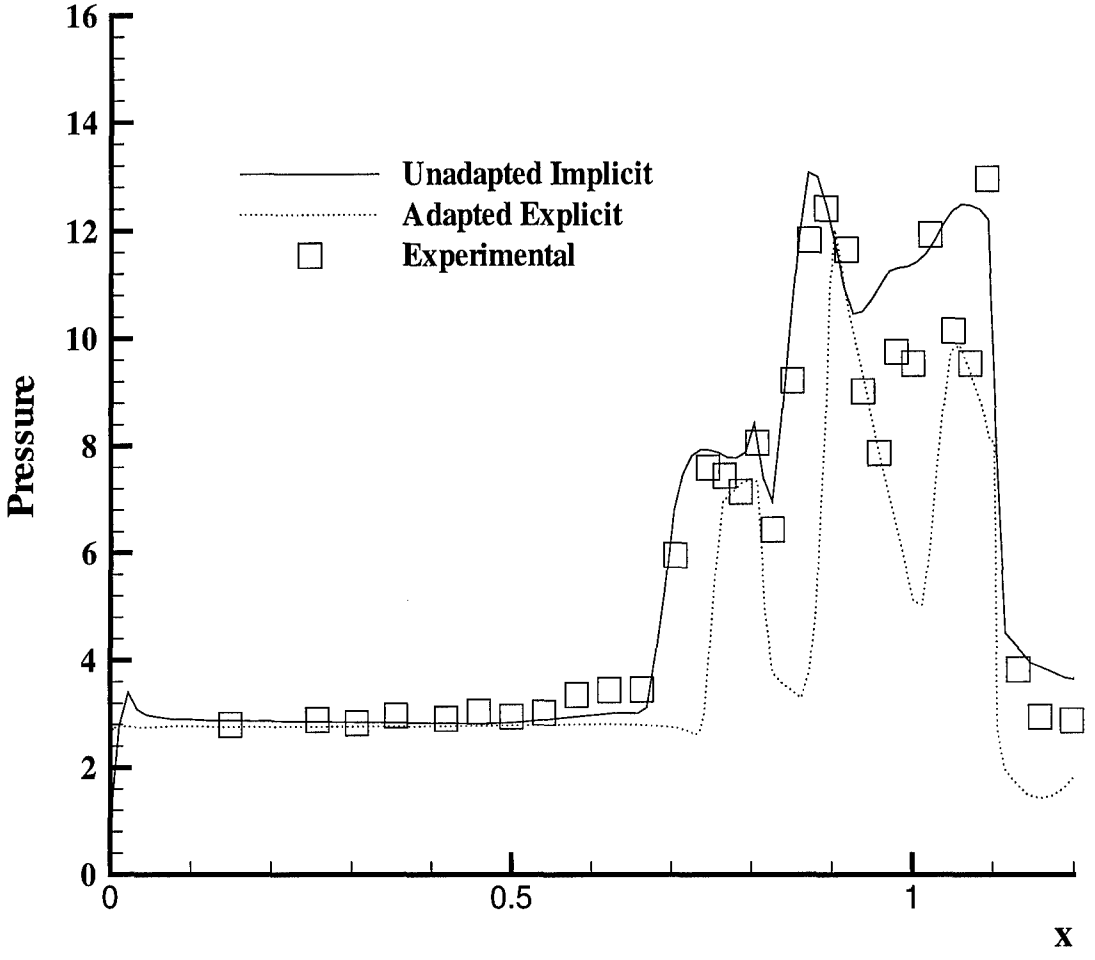

Figure 9: Pressure for Inlet–Isolator

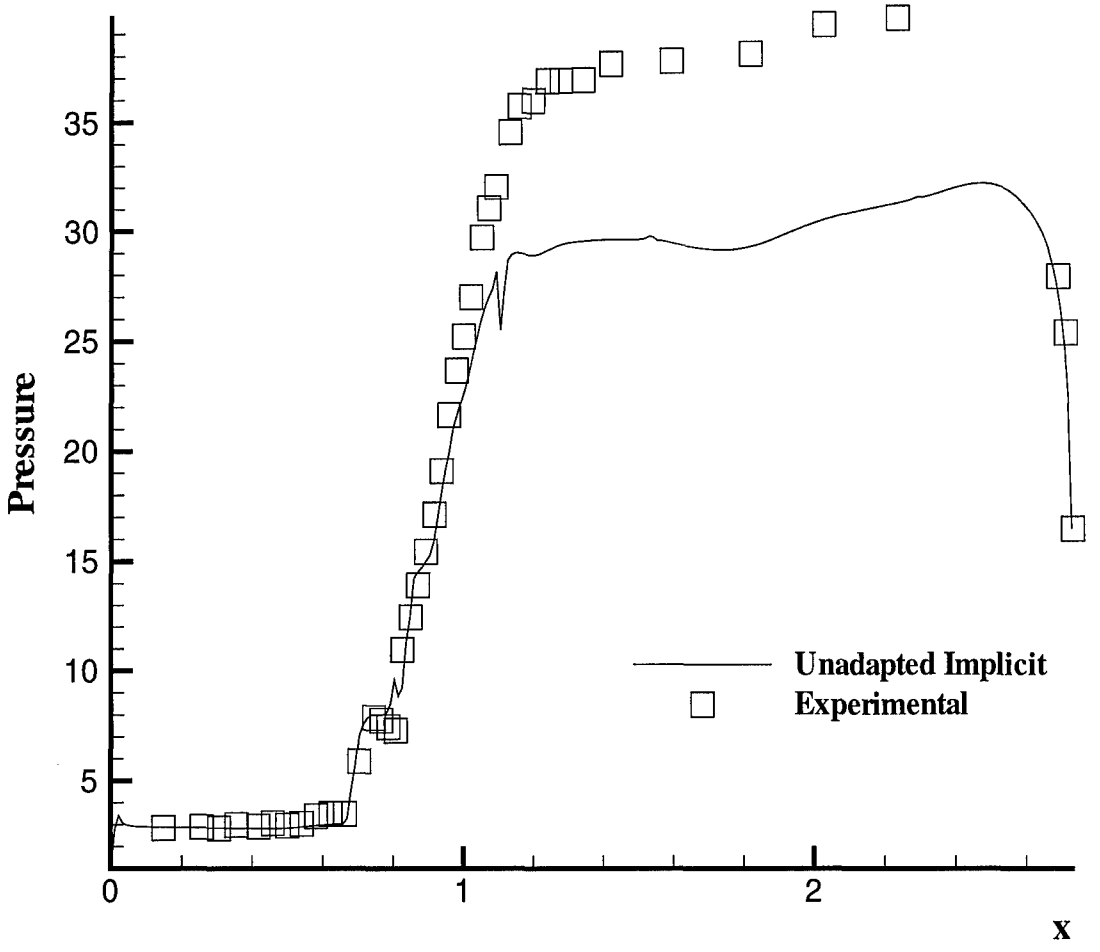

Figure 10: Pressure for Inlet–Isolator–Diffuser

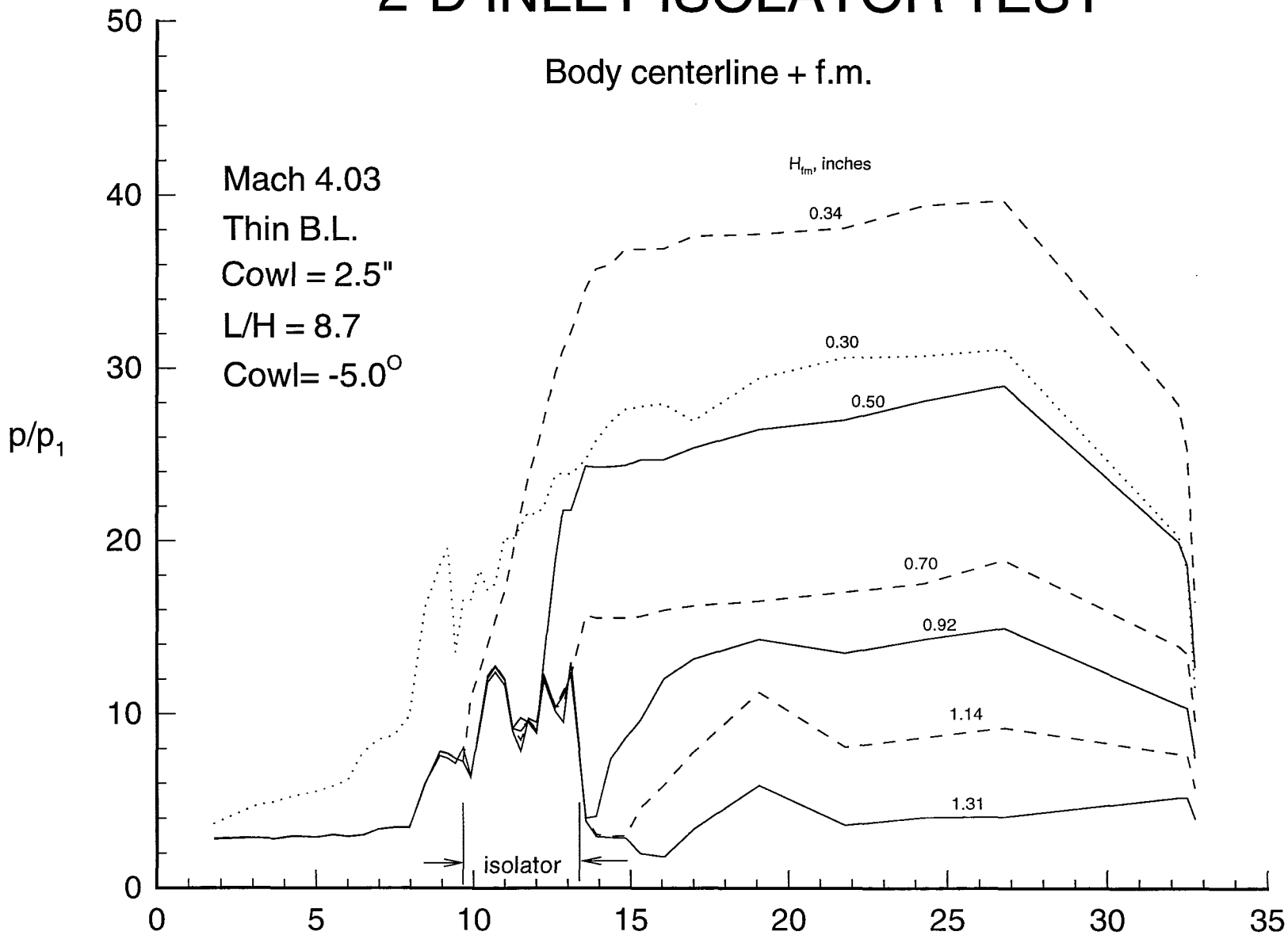

Figure 11: Inlet–Isolator–Diffuser Experiment